Conductance and gating effects at sputtered oxide interfaces

Yin, C.

4

Electron trapping mechanism in $LaAlO_3/SrTiO_3$ heterostructures

In $LaAlO_3/SrTiO_3$ heterostructures, a commonly observed but poorly understood phenomenon is that of electron trapping in back-gating experiments. In this Chapter, by combining magnetotransport measurements and self-consistent Schrödinger-Poisson calculations, we obtain an empirical relation between the amount of trapped electrons and the gate voltage. We find that the trapped electrons follow an exponentially decaying spatial distribution away from the interface. However, contrary to earlier observations, we find that the Fermi level remains well within the quantum well. The enhanced trapping of electrons induced by the gate voltage can therefore not be explained by a thermal escape mechanism. Further gate sweeping experiments strengthen our conclusion that the thermal escape mechanism is not valid. We propose a new mechanism which involves the electromigration and clustering of oxygen vacancies in $SrTiO_3$. Our work indicates that electron trapping is a universal phenomenon in $SrTiO_3$-based two-dimensional electron systems.

An adapted version of this Chapter has been submitted for publication in a peer-reviewed journal as C. Yin, A. E. M. Smink, I. Leermakers, L. M. K. Tang, N. Lebedev, U. Zeitler, W. G. van der Wiel, H. Hilgenkamp, and J. Aarts, *New insights into the electron trapping mechanism in $LaAlO_3/SrTiO_3$ heterostructures*, arXiv preprint [122].

4.1. Introduction

The capability of controlling the electronic properties of a material by applying an external voltage is at the heart of modern electronics. In particular in oxide heterostructures, there is a constant search to manipulate their novel functionalities with an externally applied electric field [2]. The most well-known example is the high-mobility two-dimensional electron system (2DES) discovered at the interface between $LaAlO_3$ and $SrTiO_3$ [9]. The 2DES exhibits intriguing physical properties, such as superconductivity [6], signatures of magnetism [10, 11, 15] and even their coexistence [7, 12]. Additionally, due to the large permittivity of the $SrTiO_3$ substrate [123], the carrier density and mobility of the 2DES can be modulated by a back-gate voltage (V_G). Gate-tunable insulator to metal transitions [26], insulator to superconductor transitions [71] and Rashba spin-orbit interactions [18, 72] have been reported. At the $LaAlO_3/SrTiO_3$ interface, the 2DES is confined in a quantum well (QW) on the $SrTiO_3$ side and the band structure is formed by the Ti t_{2g} orbitals. For $LaAlO_3$ films grown on $SrTiO_3$ (001) substrates, the d_{xy} band lies below the $d_{xz,yz}$ bands in energy [61, 89, 124]. Applying V_G across the $SrTiO_3$ substrate changes the carrier density in the QW. A Lifshitz transition occurs when the Fermi level is tuned across the bottom of the $d_{xz,yz}$ bands [63], as discussed in Chapter 1 (see Fig. 1.5).

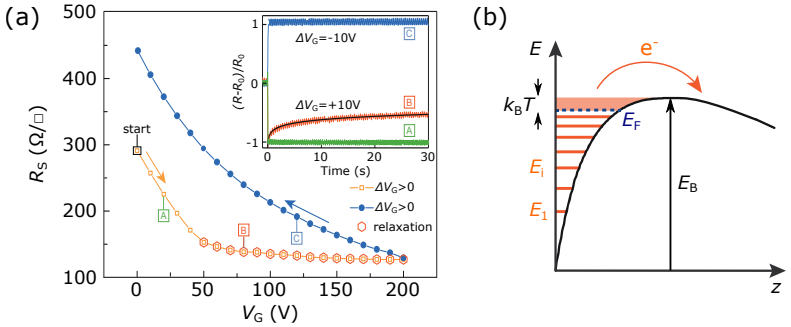

Figure 4.1: (a) Sheet resistance (R_S) as a function of gate voltage (V_G) at 4.2 K, as reported by Biscaras *et al.* [125]. Inset shows normalized resistance over time after a $\Delta V_G = \pm 10$ V step for points labeled "A", "B" and "C" in the main panel. (b) Schematic of the thermal escape mechanism where electrons escape from the quantum well beyond a filling threshold. Images adapted from Ref. [125].

In back-gating experiments, a commonly observed phenomenon is that the sheet resistance follows an irreversible route when V_G is swept first forward (increasing V_G) and then backward (decreasing V_G) [29, 71, 75, 86, 125–127], as shown in Fig. 4.1(a). The explanation as given by Biscaras *et al.* [125] is that the Fermi level lies intrinsically close to the top of the QW. High-mobility electrons escape from the QW and get trapped in $SrTiO_3$ when the carrier density is beyond a threshold, as depicted in Fig. 4.1(b). But the

relations between the amount of trapped electrons, their spatial distribution, and the back-gate voltage are still unknown.

In this Chapter, we study these relations by combining magnetotransport measurements and self-consistent Schrödinger-Poisson calculations. We find that the thermal escape mechanism cannot be reconciled with our results. We perform further gate sweeping experiments which strengthen this conclusion. We propose a new mechanism which involves the electromigration and clustering of oxygen vacancies in $SrTiO_3$.

4.2. Experiments

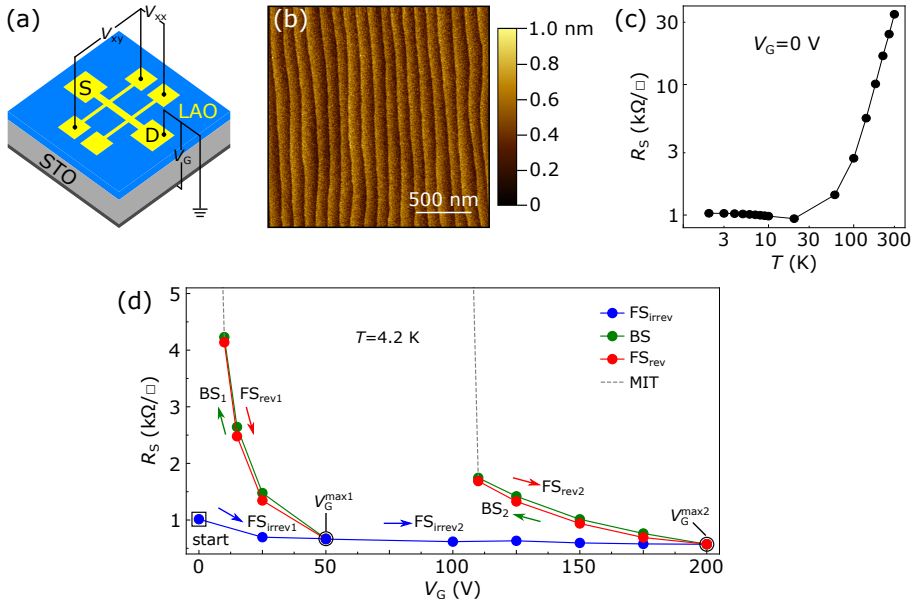

Figure 4.2: (a) Schematic of the Hall bar device. Source and drain are labeled as "S" and "D". The longitudinal voltage (V_{xx}) and transverse voltage (V_{xy}) are measured simultaneously. The gate voltage (V_G) is applied between the back of the substrate and the drain. (b) An AFM image of the $LaAlO_3$ surface taken at the Hall bar channel. (c) Temperature dependence of sheet resistance (R_s) with V_G grounded. (d) R_s as a function of V_G at 4.2 K. The solid circles are $R_s(B = 0)$. The blue, green and red arrows indicate the irreversible forward sweep (FS$_{irrev}$), backward sweep (BS), and reversible forward sweep (FS$_{rev}$), respectively. Two BSs were performed at 50 V (V_G^{max1}) and 200 V (V_G^{max2}). The gray dashed line indicates the metal-insulator transition (MIT).

The back-gating experiments were performed on a Hall bar device as depicted in Fig. 4.2(a). The Hall bar pattern was fabricated by photolithography as discussed in Chapter 2. The length between two voltage probes is 1000 µm, and the Hall bar width is 150 µm. 15 unit cells of $LaAlO_3$ film were deposited at 800 °C and an Ar pressure of 0.04 mbar by 90° off-axis sputtering. Fig. 4.2 (b) shows an AFM image of the $LaAlO_3$ surface. The back-

gate electrode was formed by uniformly applying a thin layer of silver paint (Ted Pella, Inc.) on the back of the substrate. Magnetotransport measurements were performed under different V_G at 4.2 K in the Nijmegen cryostat. The longitudinal voltage (V_{xx}) and transverse voltage (V_{xy}) were measured simultaneously by standard lock-in technique (f = 13.53 Hz and i_{RMS} = 1.0 μA). The maximum applied V_G was +200 V and the leakage current was less than 1 nA during the measurement.

The device was cooled down to 4.2 K with V_G grounded as plotted in Fig. 4.2(c). The sheet resistance R_s as a function of V_G is shown in Fig. 4.2(d). V_G was first increased from 0 V to 50 V (V_G^{max1}), resulting in a decrease of R_s. This sweep is called an irreversible forward sweep (FS_{irrev}), because R_s increased above the virgin curve when V_G was swept backward. The backward sweep (BS) led to a metal-insulator transition (MIT)[1], which is consistent with earlier reports [86]. After the onset of the MIT, defined from the phase shift of the lock-in amplifier increasing above 15°, V_G was further decreased to completely deplete the QW. When V_G was swept forward again, R_s followed the same route as the BS. Therefore the latter forward sweep is named a reversible forward sweep (FS_{rev}). Another BS was performed at 200 V (V_G^{max2}). It can be seen that R_s increased faster in BS_1 than in BS_2. The reason of which will be discussed later.

4.3. Back-gate tuning of magnetotransport properties

Fig. 4.3(a)-(h) demonstrate the back-gate tuning of magnetotransport properties in various regimes. Besides a weak antilocalization signature in low magnetic fields[2] [72] (Fig. 4.3(a)-(d)), we observed the characteristic features of the Lifshitz transition [63], namely a positive magnetoresistance, MR = $[R_s(B)/R_s(0) - 1] \times 100\,\%$, in high magnetic fields (Fig. 4.3(a)-(d)) and a nonlinear Hall resistance (Fig. 4.3(e)-(h)). To extract the carrier density and mobility as a function of V_G, we fitted the magnetotransport data with a two-band model [128]

$$R_s = \frac{1}{e} \cdot \frac{\frac{n_1\mu_1}{1+(\mu_1 B)^2} + \frac{n_2\mu_2}{1+(\mu_2 B)^2}}{\left(\frac{n_1\mu_1}{1+(\mu_1 B)^2} + \frac{n_2\mu_2}{1+(\mu_2 B)^2}\right)^2 + \left(\frac{n_1\mu_1^2 B}{1+(\mu_1 B)^2} + \frac{n_2\mu_2^2 B}{1+(\mu_2 B)^2}\right)^2}, \tag{4.1}$$

$$R_{xy} = \frac{B}{e} \frac{\frac{n_1\mu_1^2}{1+\mu_1^2 B^2} + \frac{n_2\mu_2^2}{1+\mu_2^2 B^2}}{\left(\frac{n_1\mu_1}{1+\mu_1^2 B^2} + \frac{n_2\mu_2}{1+\mu_2^2 B^2}\right)^2 + \left(\frac{n_1\mu_1^2 B}{1+\mu_1^2 B^2} + \frac{n_2\mu_2^2 B}{1+\mu_2^2 B^2}\right)^2}, \tag{4.2}$$

where n_1 and n_2 are the carrier densities of the first and second conduction bands, respectively, and μ_1 and μ_2 are the corresponding mobilities. We note that n_1 has the d_{xy}

[1] We note that the MIT can be observed in Hall bar devices, but not in unpattered samples measured by the van der Pauw method. See Fig. 4.9 in the supplemental material for more details.

[2] The weak antilocalization effect will be discussed in more detail in Chapter 5.

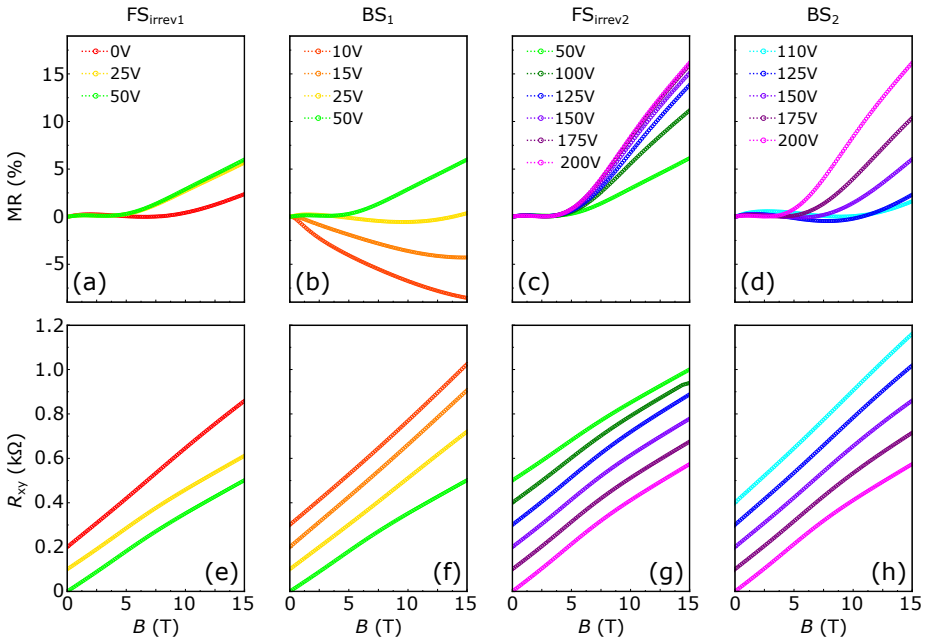

Figure 4.3: (a)-(d) Magnetoresistance, MR = $[R_s(B)/R_s(0)-1]\times 100\,\%$, as a function of magnetic field, B, in various regimes: (a) FS$_{irrev1}$, (b) BS$_1$, (c) FS$_{irrev2}$ and (d) BS$_2$. (e)-(h) Hall resistance, R_{xy}, as a function of B in various regimes: (e) FS$_{irrev1}$, (f) BS$_1$, (g) FS$_{irrev2}$ and (h) BS$_2$. Curves are separated by an offset of 100 Ω for clarity. The results of FS$_{rev}$ regimes are similar to that of BS regimes, which are therefore omitted.

character and n_2 has the $d_{xz,yz}$ character. The total carrier density, n_{tot}, is the sum of n_1 and n_2.

It can be seen in Fig. 4.4(a) and (b) that only the d_{xy} band was occupied at 0 V. In FS$_{irrev1}$, electrons were added into the QW and the Lifshitz transition occurred at a carrier density (n_L) of 1.51×10^{13} cm^{-2}, which is close to earlier reported values [63]. In BS$_1$, n_{tot} decreased to 1.33×10^{13} cm^{-2} at 10 V, which is the onset of the MIT, comparable to the earlier reported carrier density (0.5-1.5 $\times10^{13}$ cm^{-2}) for the MIT [129]. In FS$_{rev1}$, the carrier densities of the bands were tuned reversibly as in BS$_1$ and the system was fully recovered when 50 V was reapplied. In FS$_{irrev2}$, n_{tot} almost saturated at 2.17×10^{13} cm^{-2} beyond 125 V. In BS$_2$, the MIT occurred at 110 V with a carrier density of 1.65×10^{13} cm^{-2}, which could be due to the Hall bar contacts becoming insulating faster than the channel [90]. A noteworthy feature is that the amount of gate-induced trapped electrons is independent of the number of backward sweeps and is only related to V_G^{max}.

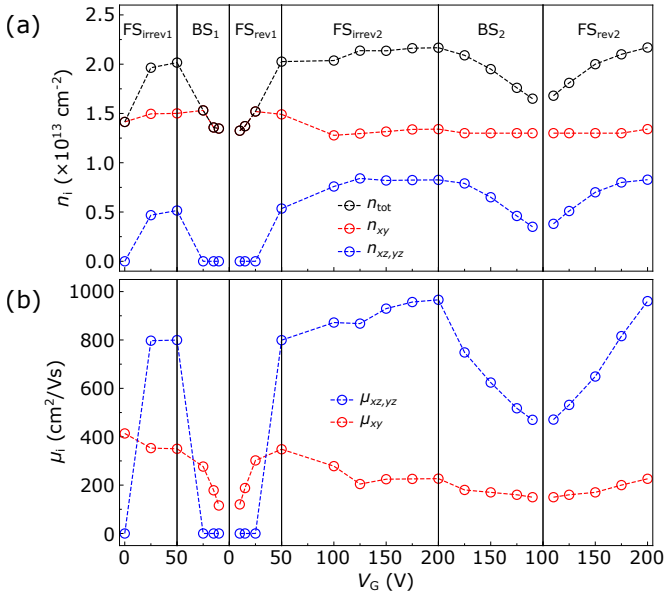

Figure 4.4: (a) Carrier density as a function of V_G in various regimes. The red and blue circles represent the carrier density of the d_{xy} band (n_{xy}) and the $d_{xz,yz}$ band ($n_{xz,yz}$). The black circle is the total carrier density (n_{tot}), which is the sum of n_{xy} and $n_{xz,yz}$. (b) Corresponding values for the mobility in various regimes.

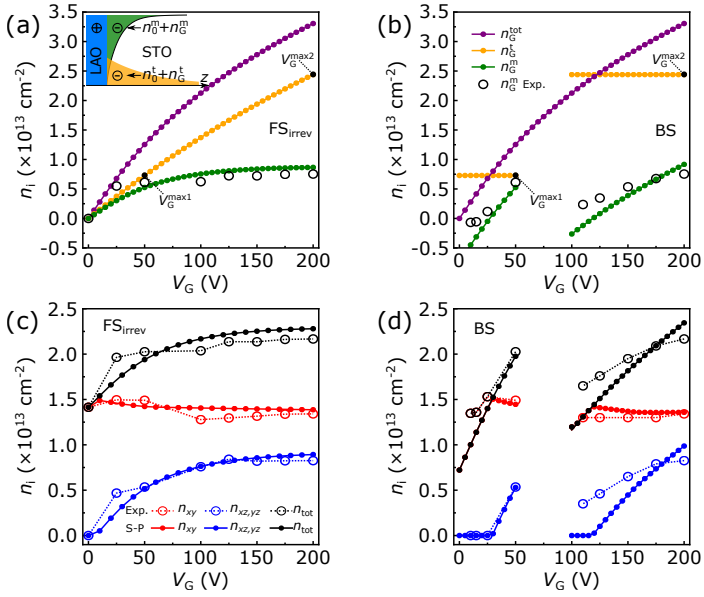

Figure 4.5: (a)-(b) V_G dependence of the calculated gate-induced total charge density (n_G^{tot}, purple), trapped charge density (n_G^{tr}, yellow), mobile charge density (n_G^{m}, green) and measured gate-induced mobile charge density (n_G^{m} Exp., open black circle) in (a) FS$_{irrev}$ and (b) BS regimes. The inset of (a) shows an illustration of the interface for Schrödinger-Poisson (S-P) calculations. (c)-(d) V_G dependence of S-P calculated (solid circles) and measured (open circles) n_{xy} (red), $n_{xz,yz}$ (blue) and n_{tot} (black) in (a) FS$_{irrev}$ and (b) BS regimes.

4.4. Schrödinger-Poisson calculations

First, we study the relation between the amount of trapped electrons and the gate voltage. In a back-gating experiment, the total amount of electrons (n_G^{tot}) induced by V_G, as shown by the purple curves in Fig. 4.5(a) and (b), can be calculated using a parallel plate capacitor model [130, 131]:

$$n_G^{tot}(V_G) = \int_{V_1}^{V_2} \frac{\epsilon_0}{e d_{STO}} \epsilon_r(V_G) dV_G, \tag{4.3}$$

where ϵ_0 is the vacuum permittivity, e is the electron charge and d_{STO} is the thickness of the $SrTiO_3$ substrate (0.5 mm). The field-dependent permittivity of the $SrTiO_3$ substrate $\epsilon_r(V_G)$ is calculated following Ref. [132]:

$$\epsilon_r(E) = 1 + \frac{B}{[1 + (E/E_0)^2]^{1/3}}, \tag{4.4}$$

where the electric field $E = V_G/d_{STO}$, $B = 25\,462$ and $E_0 = 82\,213$ V/m. In FS$_{irrev}$ regimes, as shown in Fig. 4.5(a), a part of n_G^{tot} becomes gate-induced trapped electrons (n_G^{tr}) in $SrTiO_3$. Subtracting n_G^{tr} from n_G^{tot} will give the amount of gate-induced mobile electrons

(n_G^m) which are doped into the QW. We find that the relation between n_G^{tr} and V_G can be described using the following expression:

$$n_G^{tr}(V_G) = N(1 - e^{-\frac{V_G}{400}}), \tag{4.5}$$

which yields the yellow curve, where $N = 6.2 \times 10^{13}\,cm^{-2}$. The subtraction ($n_G^{tot} - n_G^{tr} = n_G^m$) is given by the green curve, and gives a good description of the measured n_G^m (open black circle). In BS regimes, as shown in Fig. 4.5(b), n_G^{tot} is given by V_G according to Eq. (4.3). However, the value of n_G^{tr} is fixed at the $n_G^{tr}(V_G^{max})$. Thus, n_G^m is smaller than its counterpart in FS_{irrev} regimes. In both BS regimes the calculated n_G^m is in good agreement with the experimental data. Moreover, due to the field-dependent permittivity, dn_G^{tot}/dV_G is decreasing as V_G increases. As a consequence, the same negative ΔV_G removes more mobile electrons at 50 V than at 200 V, which could explain the fact that R_s increases faster in BS_1 than in BS_2. It should be noted that the empirical formula of $n_G^{tr}(V_G)$ is not universal, but instead varies among samples. We performed similar V_G sweeps on two reference samples and observed slightly different V_G dependence of R_s (See Fig. 4.10 in the supplemental material for more details.). Thus, $n_G^{tr}(V_G)$ should always be obtained from experimental results.

Next, we study the spatial distribution of the trapped electrons. The self-consistent Schrödinger-Poisson (S-P) model is a tool to study the charge distribution and band occupation [89, 128, 133–135]. S-P calculations are based on the effective mass and envelope wave function approximations[3]. Due to the orbital orientation, d_{xy} and $d_{xz,yz}$ orbitals are heavy and light in the z direction, respectively. Here, we take the effective mass as $m_{xy}^{*z} = 14\ m_e$ and $m_{xz,yz}^{*z} = 0.7\ m_e$ [89, 124, 134], where m_e is the electron rest mass. We take $z > 0$ to be $SrTiO_3$ and $z < 0$ to be $LaAlO_3$, as shown in the inset of Fig. 4.5(a). In the original state, there are initial mobile electrons (n_0^m, $1.41 \times 10^{13}\,cm^{-2}$ in our sample) and initial trapped electrons (n_0^{tr}) on the $SrTiO_3$ side, and an equivalent amount of positive charges on the $LaAlO_3$ side to keep overall charge neutrality.

The spatial distributions of the trapped electrons, both n_0^{tr} and $n_G^{tr}(V_G)$, are input parameters of the S-P model, which effectively influence the V_G dependent occupation of the d_{xy} and $d_{xz,yz}$ bands. In our calculations, we obtain the best results by using the following distribution of the trapped electrons:

$$n_{3D}^{tr}(z, V_G) = \begin{cases} 0 & \text{for } z < 0 \\ \frac{n_0^{tr} + n_G^{tr}(V_G)}{\lambda} e^{-\frac{z}{\lambda}} & \text{for } z \geqslant 0 \end{cases} \tag{4.6}$$

where $n_0^{tr} = 6.4 \times 10^{13}\,cm^{-2}$ and $\lambda = 50\,nm$. The integration range is from 0 nm to 100 nm, which is divided into 2000 equal sections. The calculated evolutions of n_{xy} and $n_{xz,yz}$ in

[3] A detailed description of the self-consistent Schrödinger-Poisson calculation can be found in Appendix A.

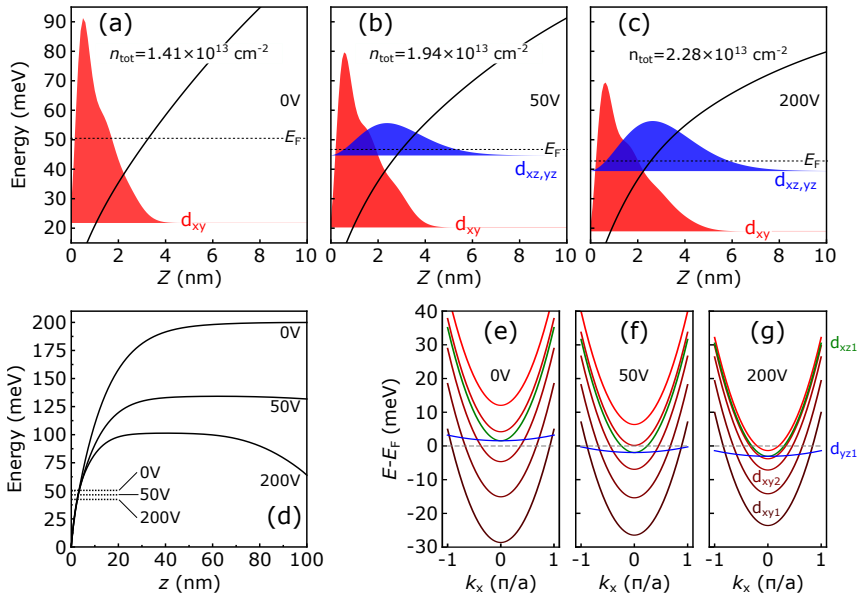

Figure 4.6: (a)-(c) S-P calculated confining potential profile (solid line), Fermi energy (dotted line), and spatial distribution of mobile electrons occupying d_{xy} (red) and $d_{xz,yz}$ (blue) bands at (a) 0 V, (b) 50 V and (c) 200 V. (d) S-P calculated confining potential profile and Fermi energy in a larger range. (e)-(f) S-P calculated subband dispersions in parabolic approximation at (e) 0 V, (f) 50 V and (g) 200 V.

FS$_{irrev}$ and BS regimes are shown in Fig. 4.5(c) and (d), closely agreeing with the experimental data.

Based on the above analysis, we could obtain the confining potential profile, the Fermi energy and the spatial distribution of mobile electrons occupying the d_{xy} and $d_{xz,yz}$ bands. Fig. 4.6(a)-(c) show the results at 0 V, 50 V and 200 V, respectively. The mobile electrons are confined within ~10 nm at the interface, which agrees with the reported spatial distribution of the 2DES [44, 136, 137]. Fig. 4.6(d) shows the confining potential in a larger range. It can be seen that in all cases the Fermi level is well below the top of the QW, therefore the probability of mobile electrons thermally escaping ($k_B T(4.2\,\text{K}) \approx 0.36$ meV) from the QW should be very low. The subband dispersions of the three cases are shown in Fig. 4.6(e)-(g). We note that increasing V_G decreases the spacing between the subband levels.

4.5. Revaluation of thermal escape mechanism

In order to check the thermal escape mechanism [125] in more detail, we warmed up the device to room temperature to remove the electron trapping effect [29]. The device

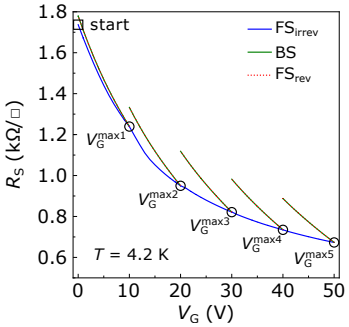

Figure 4.7: V_G dependence of R_s at 4.2 K. Backward sweeps were performed from 10 V to 50 V. Note that BS and FS_{rev} overlap perfectly.

4

was cooled down to 4.2 K again and multiple backward sweeps were performed from 10 V to 50 V. As shown in Fig. 4.7, a growing R_s separation between FS_{irrev} and BS can be clearly seen as V_G^{max} increases. In the thermal escape mechanism, it is stated that electron trapping only occurs after R_s (or n_{tot}) reaches its saturation. However, our experiment clearly shows that electron trapping occurs immediately when positive V_G is applied and the amount of trapped electrons increases as V_G^{max} increases. So we can rule out the thermal escaping of mobile electrons to be the mechanism for electron trapping. Moreover, similar irreversible behavior has been also reported in other 2DES, such as $LaTiO_3/SrTiO_3$ [125], $LaVO_3/SrTiO_3$ [75], $(LaAlO_3)_{0.3}(Sr_2AlTaO_6)_{0.7}/SrTiO_3$ [138] and amorphous $LaAlO_3/SrTiO_3$ [139]. Therefore the electron trapping phenomenon must be intrinsic to the $SrTiO_3$ substrate.

4.6. Discussion

We propose a two-step trapping mechanism which involves the redistribution of oxygen vacancies (V_Os) in $SrTiO_3$ under influence of an electric field. The first step is the electromigration of V_Os. Among all types of defects in $SrTiO_3$, V_O has the lowest activation enthalpy for migration [140]. Electromigration of V_Os in $SrTiO_3$ has also been reported in previous works [141–143]. The second step is the clustering of V_Os. It has been calculated that V_Os clustering could form in-gap trapping states [144, 145], of which the energy was recently determined to be ~0.31 eV and ~1.11 eV below the conduction band [146]. Fig. 4.8 shows the dynamic resistance change during and after V_G sweeps in the FS_{irrev} and BS regimes. The electron trapping mechanism can then be explained as follows. In FS_{irrev} regimes as shown in Fig. 4.8(a), the effect of increasing V_G is twofold. One is to add electrons into the QW. The other is to push positively charged V_Os migrating toward the interface. The clustering of the accumulated V_Os then forms in-gap trapping

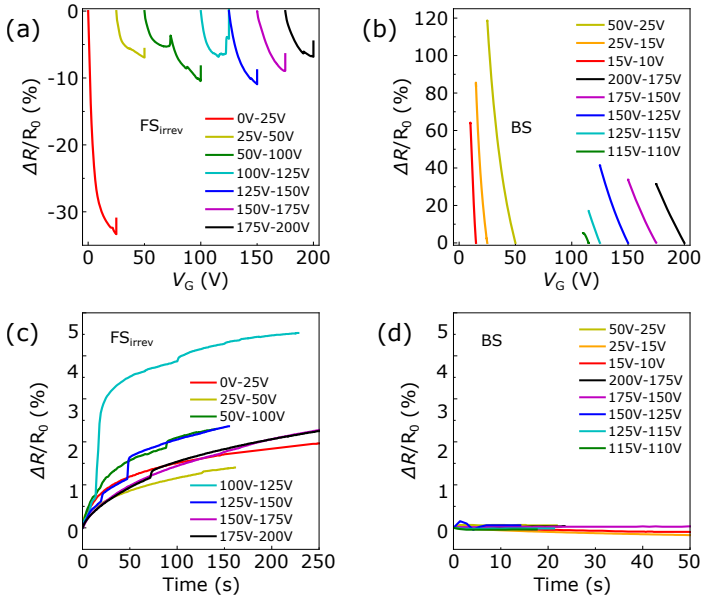

Figure 4.8: (a)-(b) Dynamic change of R_s during V_G sweeps in (a) FS$_{irrev}$ and (b) BS regimes. V_G was swept at a rate of 0.1 V/s. R_s measurements kept on going for several minutes after the stabilization of V_G. (c)-(d) Dynamic change of R_s after V_G sweeps in (c) FS$_{irrev}$ and (d) BS regimes.

states. Several sudden resistance jumps can be clearly seen during V_G sweeps, which might be due to the formation of big V_O clusters. Moreover, after stabilizing the gate voltage as shown in Fig. 4.8(c), the electromigration and clustering of V_Os do not stop immediately. Newly formed in-gap states still trap conduction electrons, resulting in an immediate increase of R_s when V_G stabilizes. In BS and FS$_{rev}$ regimes as shown in Fig. 4.8(b) and (d), sweeping V_G only changes the carrier density in the QW without modifying the defect landscape near the interface. Therefore the system can be tuned in a reversible manner.

4.7. Conclusion

In summary, we have studied the electron trapping phenomenon in $LaAlO_3/SrTiO_3$ heterostructures under back-gate voltages. By combing magnetrotransport measurements and self-consistent Schrödinger-Poisson calculations, we have identified a relation between the amount of trapped electrons and the gate voltage as well as the spatial distribution of the trapped electrons. We have proposed a new trapping mechanism which involves the electromigration and clustering of oxygen vacancies in $SrTiO_3$, since our analysis shows that the thermal escape mechanism is not valid. Our work improves

the understanding of back-gating experiments in $LaAlO_3/SrTiO_3$ heterostructures. It is also valuable for theoretical works [134, 147, 148], where the assumption was that all the gate-induced electrons land in the QW. This assumption clearly needs to be reconsidered. Equally importantly, our work indicates that electron trapping is a universal phenomenon in $SrTiO_3$-based two-dimensional electron systems, which is instructive to future applications of complex oxide electronic devices.

Supplemental material

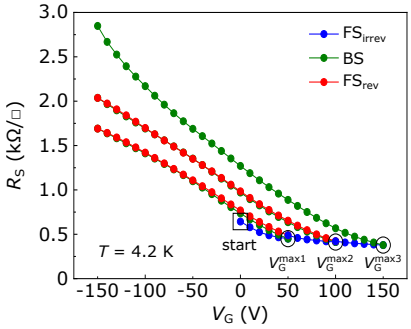

Figure 4.9: Sheet resistance (R_S) as a function of gate voltage (V_G) at 4.2 K measured on an unpatterned sample by the van der Pauw method. Backward sweeps performed at 50 V, 100 V and 150 V, respectively.

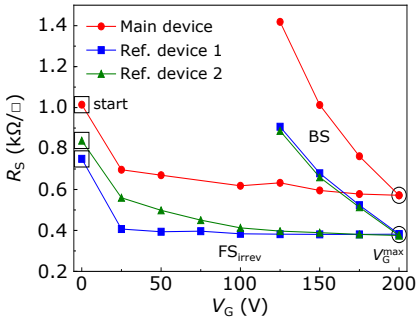

Figure 4.10: Sheet resistance (R_S) as a function of gate voltage (V_G) at 4.2 K measured on two reference devices. Backward sweep performed at 200 V.